Ceramics International xxx (xxxx) xxx–xxx

Contents lists available at ScienceDirect

Ceramics International

journal homepage: www.elsevier.com/locate/ceramint

Phase evolution, structure and microwave dielectric properties of $Li_{2+x}Mg_3SnO_6$ (x = 0.00–0.12) ceramics

Zixuan Fang[a,b], Bin Tang[a,b,*], Feng Si[a,b], Enzhu Li[a,b], Hongyu Yang[a,b], Shuren Zhang[a,b]

[a] National Engineering Center of Electromagnetic Radiation Control Materials, Univer sity of Electronic Science and Technology of China, Jianshe Road, Chengdu 610054, PR China

[b] State Key Laboratory of Electronic Thin Films and Integrated Devices, University of Electronic Science and Technology of China, Jianshe Road, Chengdu 610054, PR China

ARTICLE INFO

Keywords:
Microwave Dielectrics Ceramics
High Q
Atmosphere-Controlled Sintering

ABSTRACT

In this study, the $Li_{2+x}Mg_3SnO_6$ (LxMS) ceramic systems were prepared by solid-state reaction using novel atmosphere-controlled sintering (x = 0.00–0.12). The influences of extra lithium contents on the phase evolution, crystal structure and microwave dielectric properties of $Li_{2+x}Mg_3SnO_6$ (LxMS) ceramics were systematically investigated. As samples were calcined from 800 to 1000 °C, the $Li_2Mg_3SnO_6$ phase was formed from the chemical reaction between Li_2SnO_3 and MgO phase. Pure $Li_2Mg_3SnO_6$ phase could be observed for samples calcined at 1000–1100 °C. But when it was exposed to high temperature air over 1100 °C, the $Li_2Mg_3SnO_6$ decomposed into Mg_2SnO_4, MgO and Li_2O. Because of the protective atmosphere and extra lithium, the ε_r, $Q\times f$ and τ_f were significantly improved by the suppression of secondary phase and pores for $0.00\leq x\leq 0.08$. However, comprehensive microwave characteristics were deteriorated for $0.08<x\leq 0.12$, which were correlated with dielectric polarization, bond valence, FWHM, packing fraction and octahedral distortion. The excellent microwave characteristics of LxMS (x = 0.08) sintered at 1350 °C in novel controlled atmosphere were obtained: ε_r = 12.7, $Q\times f$ = 168,330 GHz and τ_f = −27.4 ppm/°C.

1. Introduction

Because of rapid growth in the wireless communication market, microwave dielectric ceramics have played an irreplaceable role as key components in the microwave devices ranging from any hand-held terminals to base stations [1,2]. To meet the specific request of fifth-generation (5G) communication and applications [3–5], these ceramics need to have the desired dielectric constant (ε_r), high quality factor ($Q\times f$) and adjustable temperature coefficient of the resonant frequency (τ_f). The exploration of new microwave materials by novel approach and investigation of the correlation between structures and microwave dielectric characteristics have always been the center of material research [6,7].

The $Li_2Mg_3BO_6$ (B = Ti, Zr, Sn) ceramics with rock-salt structure have attracted considerable attentions due to their excellent performance at microwave frequencies ($Li_2Mg_3TiO_6$: ε_r = 15.2, $Q\times f$ = 152,000 GHz, and τ_f = −39 ppm/°C; $Li_2Mg_3SnO_6$: ε_r = 8.8, $Q\times f$ = 123,000 GHz, and τ_f = -32 ppm/°C; $Li_2Mg_3ZrO_6$: ε_r = 12.6, $Q\times f$ = 86,000 GHz, and τ_f = -36 ppm/°C) [8–10]. The appearance of secondary phase Mg_2SnO_4 (ε_r = 8.41, $Q\times f$ = 55,100 GHz, and τ_f = −62 ppm/°C [11]) and pores caused by lithium volatilization in $Li_2Mg_3SnO_6$ made it inferior to $Li_2Mg_3TiO_6$ and $Li_2Mg_3ZrO_6$ ceramics. And the porous microstructure caused by the loss of Li element would seriously deteriorate the quality factor, which also was detrimental for $Li_2Mg_3BO_6$ to be practically used in the microwave circuits [12,13]. Thus, how to combat the lithium volatilization was one of main issues to obtain the best microwave dielectric characteristics. Some efforts have been made to “cure” the lithium volatilization in lithium containing materials. Among these researches, Wu *et al.* only described that pure $Li_2Mg_3TiO_6$ and $Li_2Mg_3ZrO_6$ phase could be prepared through burying the samples in Li-containing sacrificial powder [9]. The low temperature additives are usually used to reduce the sintering temperature of ceramic systems; therefore, the lithium volatilization can be relieved to a certain extent, but this will seriously damage the microwave dielectric characteristics, especially ε_r and $Q\times f$ values [14,15].

However, there were not any systematic studies on curing lithium volatilization in the $Li_2Mg_3SnO_6$ ceramics by an effective and reliable method; this was the possible reason that there were not any further studies of the $Li_2Mg_3SnO_6$ ceramics due to their sintering difficulties.

* Corresponding author at: National Engineering Center of Electromagnetic Radiation Control Materials, State Key Laboratory of Electronic Thin Films and Integrated Devices, University of Electronic Science and Technology of China, Jianshe Road, Chengdu 610054, PR China.
E-mail address: tangbin@uestc.edu.cn (B. Tang).

http://dx.doi.org/10.1016/j.ceramint.2017.07.074
Received 4 June 2017; Received in revised form 29 June 2017; Accepted 10 July 2017

Thus, the importance of suppression of secondary phase and pores could not be overemphasized for $Li_2Mg_3SnO_6$ ceramics. In this work, the chemical stable ZrO_2 powders were used as the protective material for the $Li_{2+x}Mg_3SnO_6$ (x = 0.00–0.12) samples to be buried in and Li_2CO_3 powders were used to provide the Li-rich sintering atmosphere, which was a brand new sintering method for microwave ceramics. The well-established technique of sintering under a powder bed using sacrificial powder was to control the local atmosphere. Moreover, the phase evolution, sintering behaviors and microwave dielectric properties of $Li_{2+x}Mg_3SnO_6$ (x = 0.00–0.12) ceramics were investigated by XRD, SEM, Rietveld refinement, and Raman spectra technology in details.

2. Experimental procedure

The initial raw materials with at least 99.5% purity ($(Mg(OH)_2 \cdot 4MgCO_3 \cdot 5H_2O$, Li_2CO_3 and SnO_2) were used to prepare the $Li_{2+x}Mg_3SnO_6$ powders. The raw powders were weighed as $Li_{2+x}Mg_3SnO_6$ (LxMS), where x = 0.00, 0.04, 0.08, 0.12 and 0.25, and were ball milled in a nylon jar with zirconia balls in ethanol for 7 h. The resulting mixtures for x = 0.00–0.25 were dried and calcined at 900 °C for 4 h. Specifically, mixture for x = 0.08 were calcined from 200 °C to 1300 °C with the step size of 100 °C. Then, the calcined powders at 900 °C were reground for 5 h, dried, mixed with a 6 wt% of a 10% solution of polyvinyl alcohol (PVA) as a binder and granulated. The obtained powder was axially pressed into cylindrical disks with a thickness of 7.25 mm and a diameter of 14.5 mm under a pressure of 200 N/m^2. A part of $Li_{2+x}Mg_3SnO_6$ (x = 0.00, 0.04, 0.08, 0.12 and 0.25) were sintered at 1350 °C for 5 h in air with heating and cooling rate of 6 °C/min. As schematically shown in Fig. 1, the rest of $Li_{2+x}Mg_3SnO_6$ (x = 0.00, 0.04, 0.08 and 0.12) were sintered from 1300 °C to 1400 °C with a step size of 25 °C for 5 h in controlled-atmosphere at heating and cooling rate of 6 °C/min.

The bulk densities of the LxMS ceramics were measured using the Archimedes' principle. Powder phase compositions were examined by X-ray diffraction (XRD) using CuKα radiation (Philips x'pert Pro MPD, Netherlands), and the refined lattice parameters of the samples were analyzed by GSAS suite with EXPGUI software [16]. In this software, the reliability was evaluated by three factors (R_{wp}-reliability factor of weighted patterns, R_p-reliability factor of patterns, $\times^2$-goodness of fit indicator). The schematic illustration of $Li_{2+x}Mg_3SnO_6$ (x = 0.08) crystals was drawn by VESTA. Scanning electron microscopy (SEM) and energy dispersive X-ray spectroscopy (EDX) (HITACHI S-9220, Japan) were employed to study the thermally etched surface photograph of the LxMS ceramics. We collected data of Raman spectra by Horiba Jobin–Yvon HR800 UV Raman spectrometer, and the data were analyzed by professional Labspec5. The 532.08 nm line of He–Ne laser source was used as the exciting wavelength for $Li_{2+x}Mg_3SnO_6$ (x = 0.00, 0.04, 0.08 and 0.12) ceramics. The ε_r and $Q \times f$ values of the polished samples at 9–12 GHz were measured by a network analyzer (Agilent Technologies E5071C, USA) using the Hakki–Coleman dielectric resonator method in TE011 mode and temperature chamber (DELTA 9023, Delta Design, USA). The τ_f was calculated from data obtained in the temperature range of 25–85 °C according to the

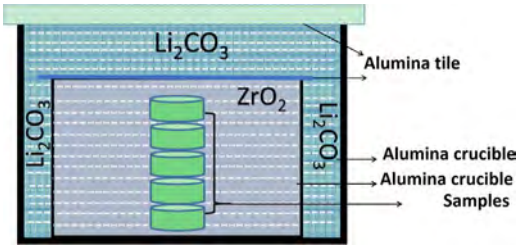

Fig. 1. Schematic representation of the $Li_{2+x}Mg_3SnO_6$ (x = 0.00–0.12) placement for providing ZrO_2-burying protective atmosphere and Li-rich atmosphere.

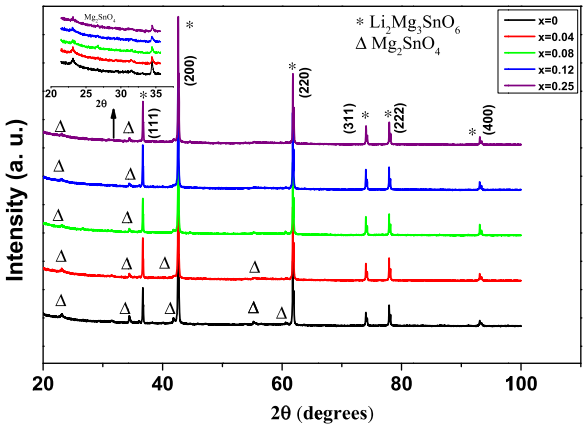

Fig. 2. Powder XRD patterns of $Li_{2+x}Mg_3SnO_6$ (x = 0.00–0.25) ceramics sintered at 1300 °C for 5 h in air.

equation:

$$\tau_f = (10^6 \times \Delta f / (f_{t_1} \times \Delta T)), \quad (1)$$

where f_{t_1} is the resonant frequencies at the measuring temperature t_1 (25 °C).

3. Results and discussion

Before discussing the results of investigation, we have studied the effects of extra lithium on microstructures and microwave dielectric characteristics of $Li_{2+x}Mg_3SnO_6$ (x = 0.00, 0.04, 0.08, 0.12 and 0.25) ceramics sintered in air and introduced the atmosphere-controlled sintering. Fig. 2 shows the normalized XRD patterns of $Li_{2+x}Mg_3SnO_6$ (x = 0.00–0.25) ceramics sintered at 1300 °C for 5 h in air, and the top-left inset in Fig. 2 presents the amplified profiles of the diffraction peaks around the 2θ angle of 25.5°. The main crystalline phase of all samples were identified as standardized pattern of cubic $Li_2Mg_3SnO_6$ (JCPDS#39-0932). However, the Mg_2SnO_4 phase (JCPDS #74-2152) existed in all composition ranges. With the increase of Li contents, the intensity of Mg_2SnO_4 phase became lower; this indicated that the extra of lithium could help inhibit the appearance of Mg_2SnO_4 phase. Table 1 lists the microwave dielectric properties of LxMS (x = 0.00–0.25) ceramics versus extra lithium compositions. The microwave dielectric properties of LxMS (x = 0.00–0.25) ceramics were not improved by the extra lithium because of serious lithium volatilization. Later, we also directly provided Li-rich atmosphere for samples or buried them in sacrificial powders of the same composition. But the LxMS (x = 0.00–0.25) samples either melted in a Li-rich atmosphere or had chemical reaction with the sacrificial powders (refer to attached Supplementary Fig. 1). We were not able to prepare samples for testing. Based on previous work, it was very necessary to find a stable and controllable material to work as the protective material, and find a material to work as sacrificial powder. The power bed was widely used to control the local atmosphere in the manufacturing technology [17,18]. The chemical stable ZrO_2 powder was chosen and worked as the powder bed,

Table 1
The microwave dielectric properties of $Li_{2+x}Mg_3SnO_6$ (x = 0.00–0.25) ceramics sintered in air atmosphere.

Composition (x)	ε_r	$Q \times f$(GHz)	τ_f(ppm/°C)
x = 0.00	7.04	73,711	−49.5
x = 0.04	7.18	74,710	−47.7
x = 0.08	7.29	83,174	−47.3
x = 0.12	7.45	85,345	−46.8
x = 0.25	7.31	79,960	−45.9

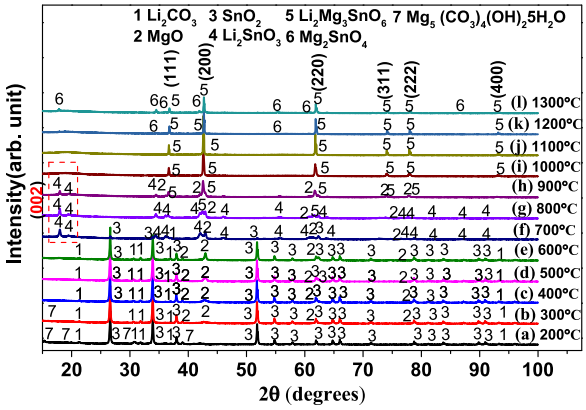

Fig. 3. XRD patterns of $Li_{2+x}Mg_3SnO_6$ (x = 0.08) powders calcined in air from 200 °C to 1300 °C for 4 h.

and Li_2CO_3 powder was used to provide Li-rich sintering atmosphere in high temperature over 1100 °C. Fig. 1 illustrates schematic representation of the $Li_{2+x}Mg_3SnO_6$ (x = 0.00–0.12) placement for providing ZrO_2-burying and Li-rich sintering atmosphere.

In the following part, the microwave dielectric properties of $Li_{2+x}Mg_3SnO_6$ (x = 0.00, 0.04, 0.08 and 0.12) ceramics sintered in controlled-atmosphere would be discussed. Fig. 3(a)~(l) illustrates the normalized XRD patterns of $Li_{2+x}Mg_3SnO_6$ (x = 0.08) powders calcined in air from 200 °C to 1300 °C for 4 h. When samples calcined at 200 °C, raw materials $Mg_5(CO_3)_4(OH)_2{\cdot}5H_2O$ (JCPDS#29-0858), Li_2CO_3 (JCPDS#87-0728) and SnO_2 (JCPDS#41-1445) were detected. As the calcination temperature reached 300 °C, $Mg_5(CO_3)_4(OH)_2{\cdot}5H_2O$ decomposed into MgO, CO_2 and H_2O, and new MgO (JCPDS#89–7746) phase formed. When the temperature was set at 600 °C, the intensity of MgO phase became larger, and there were no changes for the Li_2CO_3 and SnO_2 phase. As the calcination temperature reached 700 °C, the Li_2SnO_3 (JCPDS#31–0761) with monoclinic rock salt structure in C2/c space group was obtained for the first time, the intensity of SnO_2 became lower, and the Li_2CO_3 disappeared. This finding meant that there was a chemical reaction between Li_2CO_3 and SnO_2 when samples were calcined in the temperature range of 600 °C~700 °C, and Li_2SnO_3 and MgO could co-exist at 700 °C. However, a new phase, $Li_2Mg_3SnO_6$ (JCPDS#39-0932), with cubic rock salt structure in Fm$\bar{3}$m space group began to form when the samples were calcined at 800 °C. As the temperature increased to 900 °C, the intensity of $Li_2Mg_3SnO_6$ phase became larger at the cost of weakening Li_2SnO_3 and MgO. It was remarkable that two characteristic peaks of the Li_2SnO_3 phase around the 2θ angle of 20.0° gradually lowered with temperature from 700 °C to 900 °C. The intensity of long range ordering (LRO) degree of cations [19] indicated by (0, 0, 2) peak decreased, and finally disappeared when temperature was over 900 °C. This finding was similar to our investigation of phase evolution in $Li_2Mg_{3-x}Ca_xTiO_6$ system (x = 0.00–0.18) [8], indicating that the Li_2SnO_3 phase changed from a monoclinic rock salt structure (C2/c space group) to a cubic rock salt structure (Fm$\bar{3}$$m$ space group). Bian et al. [12] also revealed a similar mechanism in the (1−y)Li_2TiO_3 + yMgO systems with rock salt structure ($0 \le y \le 0.5$). As mentioned above, Li_2SnO_3 and MgO belonged to a big family of rock salt structure [15]. The cation sizes of Li_2SnO_3 and MgO were very similar; the ionic radii of the cations were $R(Mg^{2+})$ = 0.72Å and R[average(Li, Sn)] = 0.737Å(CN = 6)[20], respectively. The difference (∇R) between $R(Mg^{2+})$ and R[average(Li, Sn)] was calculated as 2.3%, which was much less than 15%. Thus, MgO and Li_2SnO_3 were able to form continuous solid solutions. The substitution equation could be written as,

$$Li_2SnO_3 \xrightarrow{MgO} 2Li'_{Mg} + Sn^{\bullet\bullet}_{Mg} + 3O_o, \quad (2)$$

where Li and Sn occupied the Mg site. Hence, the Li_2SnO_3 phase changed from a monoclinic rock salt structure in C2/c space group to a cubic rock salt structure in Fm$\bar{3}$$m$ space group, later became the $Li_2Mg_3SnO_6$ phase with cubic rock salt structure in Fm$\bar{3}$$m$ space group. Pure $Li_2Mg_3SnO_6$ phase could be observed at 1000 °C and 1100 °C. When the specimens were calcined at 1200 °C, the weak secondary phase could be recognized as Mg_2SnO_4 (JCPDS#74–2152), and this was due to the serious lithium volatilization when the samples were exposed to high temperature air over 1100 °C [21]. As the temperature was increased to 1300 °C, the intensity of Mg_2SnO_4 became much larger due to the decomposition of $Li_2Mg_3SnO_6$ phase. As a result, the phase evolution in $Li_{2+x}Mg_3SnO_6$ system can be expressed as follows according to Fig. 3:

$$Mg(OH)_2{\bullet}\,4MgCO_3\,{\bullet}5H_2O \xrightarrow{200°C\sim300°C} 5MgO + 4CO_2\uparrow + 6H_2O\uparrow \quad (3)$$

$$Li_2CO_3 + SnO_2 \xrightarrow{600°C\sim700°C} Li_2SnO_3(\text{monoclinic(C2/c)}) + CO_2\uparrow \quad (4)$$

$$Li_2SnO_3(\text{monoclinic(C2/c)}) + MgO(\text{cubic(Fm}\bar{3}\text{m)}) \xrightarrow{700°C\sim800°C} Li_2SnO_3 (\text{monoclinic(C2/c)}) \quad (5)$$

$$Li_2SnO_3(\text{monoclinic(C2/c)}) + MgO \xrightarrow{800°C\sim900°C} Li_2SnO_3(\text{cubic(Fm}\bar{3}\text{m)}) \quad (6)$$

$$Li_2SnO_3(\text{cubic(Fm}\bar{3}\text{m)}) + 3MgO(\text{cubic(Fm}\bar{3}\text{m)}) \xrightarrow{900°C\sim1000°C} (\text{cubic(Fm}\bar{3}\text{m)}) \quad (7)$$

$$Li_2Mg_3SnO_6(\text{cubic(Fm}\bar{3}\text{m)}) \xrightarrow{1100°C\sim1300°C} Mg_2SnO_4(\text{cubic(Fm}\bar{3}\text{m)}) + MgO(\text{cubic(Fm}\bar{3}\text{m)}) + Li_2O\uparrow \quad (8)$$

However, according to Eq. (8), MgO phase cannot be found in the samples sintered over 1100 °C. This was because that the MgO would react with $Li_2Mg_3SnO_6$ further, and finally formed the $Li_2Mg_3SnO_6$-like phase which could be confirmed in another study by us (refer to attached Supplementary Fig. 2).

Fig. 4 presents the normalized XRD patterns of $Li_{2+x}Mg_3SnO_6$ (x = 0.00–0.12) ceramic powders sintered in controlled atmosphere at optimal temperatures for 5 h. At x = 0.00, the characteristic peaks of $Li_2Mg_3SnO_6$ (JCPDS#39-0932) were indexed as (1, 1, 1), (2, 0, 0), (2, 2, 0), (3, 1, 1), and (4, 0, 0). And the peaks ((1, 1, 1), (2, 0, 0), (2, 2, 0), (3, 1, 1)) were very close to those of MgO (JCPDS#89-7746). Meanwhile, the Mg_2SnO_4 phase was also observed at x = 0.00. When Li contents (x >0.00) increased, the intensity of Mg_2SnO_4 (JCPDS#74-2152) decreased significantly, and the pure $Li_2Msg_3SnO_6$ phase formed as more lithium added ($x \ge 0.08$). This finding indicated that extra lithium could effectively compensate for lithium loss, and finally suppressed the formation of the secondary phase in the controlled atmosphere.

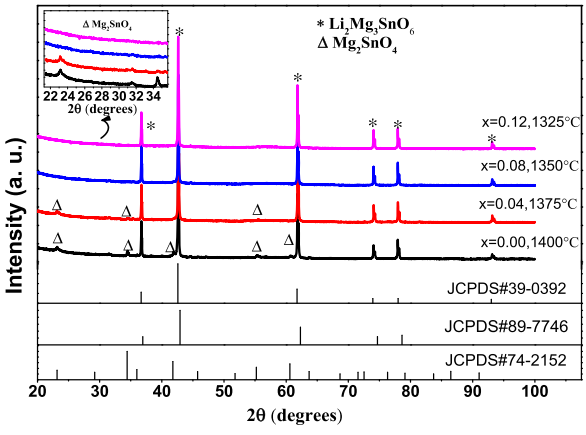

Fig. 4. Powder XRD patterns of $Li_{2+x}Mg_3SnO_6$ (x = 0.00–0.12) ceramics sintered in controlled atmosphere at optimal temperatures for 5 h.

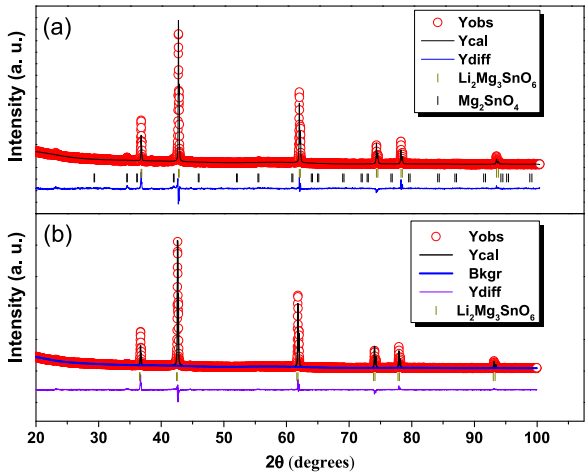

Fig. 5. The representative plots of experimental (red circle) and calculated (black line) X-ray powder diffraction for $Li_{2+x}Mg_3SnO_6$ ceramics sintered at optimal temperatures for 5 h with (a) x = 0.04 and (b) x = 0.08. (For interpretation of the references to color in this figure legend, the reader is referred to the web version of this article.)

Rietveld refinement was carried out on the fine XRD data to analyze the phase compositions in $Li_{2+x}Mg_3SnO_6$ (x = 0.00–0.12) ceramics. Fig. 5 shows the representative plots of the experimental (red circle) and calculated (black line) XRD data for $Li_{2+x}Mg_3SnO_6$ ceramics sintered at optimal temperatures for 5 h with (a) x = 0.04 and (b) x = 0.08. The experimental data were in good agreement with the calculated X-ray diffraction data. Table 2 summarizes the crystallographic data from Rietveld refinement of $Li_{2+x}Mg_3SnO_6$ (x = 0.00–0.12) ceramics sintered in controlled atmosphere. The refinement factors of R_{wp}, R_p, and $\times^2$ were in the range of 5–7%, 3–5%, and 2–3, respectively, thus our structure models were established with high reliability. The cell volume (V) of the $Li_{2+x}Mg_3SnO_6$ decreased with increasing Li contents (x = 0.00–0.08), and this was attributable to the compensation of the lithium loss in those samples. When excess lithium contents were added (x = 0.12), the cell volume (V) increased slightly. With increasing x, the weight fraction of $Li_2Mg_3SnO_6$ (M_1) increased from 95.81% to 100% whereas that of Mg_2SnO_4 (M_2) decreased from 4.19% to 0. Based on the refined data, we also provided the schematic illustration of the supercell structure (2 × 2 × 2) for $Li_{2+x}Mg_3SnO_6$ ceramic (x = 0.08), as shown in Fig. 6. According to the supercell structure and refined data, the primitive cell was composed of two $Li_{2+x}Mg_3SnO_6$ molecules, and the Li/Mg/Sn cations were coordinated with six oxygen atoms where the Li/Mg/Sn cations held 4a Wyckoff positions and oxygen ions occupied 4b Wyckoff positions. The occupancies of Li/Mg/Sn cations were 1/3, 1/2 and 1/6, and that of oxygen ions was 1.

The Raman spectra was utilized to better understand the correlations between the crystal structures and properties of the microwave dielectric ceramics. The Raman spectra of $Li_{2+x}Mg_3SnO_6$ (x = 0.00–0.12)) ceramics sintered at optimal temperatures in controlled atmosphere for 5 h are plotted in Fig. 7. It is generally considered that Raman shift and the full-width-at-half maximum (FWHM) are closely correlated with the microwave dielectric characteristics, and the Raman spectrum is also sensitive to the secondary phase [22–25]. The weak Raman peaks were found at around 640.1 cm^{-1}, 599.01 cm^{-1}, 476.42 cm^{-1} and 407.35 cm^{-1} with x = 0.00. Although same peaks could be observed at x = 0.04, it was clear that the peak at 642.44 cm^{-1} became stronger, and intensities of peaks at 476.42 cm^{-1} and 407.35 cm^{-1} decreased greatly. With x increasing from 0.08 to 0.12, peaks at 476.42 cm^{-1} and 407.35 cm^{-1} disappeared, and only one peak was observed to be located at approximately 643 cm^{-1} because of the high symmetry of LxMS crystals [9]. The single Raman peak at around 643 $cm^{-1}$was in good agreement with the reports of Li_2SnO_3 ceramics co-doped with MgO–LiF by Fu et al. [13]. Thus, we concluded that the peak at around 643 cm^{-1} was related to the vibration mode of the $Li_2Mg_3SnO_6$ crystal, and peaks at 599.01 cm^{-1}, 476.42 cm^{-1} and 407.35 cm^{-1} were related to the vibration modes of the secondary phase. It was remarkable that the peak at around 643 cm^{-1} had a blue shift from 640.15 cm^{-1} to 645.31 cm^{-1} with extra Li in the range of 0.00–0.08, but it presented a hypsochromic shift to lower 642.23 cm^{-1} at x = 0.12. These findings might be caused by the compensation of Li loss and extra Li diffusing into the crystals, which was highly correlated to the variation of cell volume. The FWHM of spectra obtained from the Lorentz fitting were 38.72 cm^{-1}, 38.18 cm^{-1}, 35.87 cm^{-1} and 36.16 cm^{-1} for x = 0.00, 0.04, 0.08 and 0.12, respectively.

To better understand the difference between microstructures at different atmosphere, Fig. 8 presents SEM of surface images of corresponding $Li_{2+x}Mg_3SnO_6$ (x = 0.00–0.12) ceramics sintered at 1350 °C for 5 h in air with (a) x = 0.00, (b) x = 0.04, (c) x = 0.08, (d) x = 0.12; SEM images of thermally etched surface of LxMS ceramics sintered at their optimal temperatures for 5 h in controlled atmosphere with (e) x = 0.00, (f) x = 0.04, (g) x = 0.08, (h) x = 0.12 and SEM images of fractured surface for x = 0.08 in controlled atmosphere (i). According to Fig. 8a~d, all specimens showed extremely porous microstructure, and no complete grains or clear grain boundaries existed, which would seriously deteriorate the microwave dielectric properties [10,21,26–28]. However, as shown in Fig. 8e, the grains and clear grain boundaries could be observed at x = 0.00. But two kinds of grains (the small oval grain A and large matrix grain B) appeared. At the same time, large amounts of pores were also found to locate at the boundaries due to the Li volatilization in high temperature. In the range of 0.04–0.12, the dense microstructures showed good grains with clear boundaries, and only matrix grains (B, C, D, E, F) could be found when additional Li was added (x ≥0.04). With the addition of lithium, the grain growth was observed for x ≥0.04. The samples sintered in controlled atmosphere had much better growing surroundings than that exposed to air, as shown in Fig. 8a~8d respectively. According to Fig. 8i, the fractured photograph of LxMS with x = 0.08 presented an absolutely dense microstructure. This finding was quite different from many literatures [9,12,21,29] in which the traces of lithium volatilization indicated by minor pores could be found in their fractured images. Table 3 lists the EDX data of marked grains that corresponds to Fig. 8. As shown in Table 3 and Fig. 8, the atomic ratio of Mg: Sn for small oval grain (A) was close to 2:1 while the ratios of Mg: Sn in matrix grains (B, C, D, E, F) were around 3:1. Thus, the

Table 2
Crystallographic data from Rietveld refinement of $Li_{2+x}Mg_3SnO_6$ (x = 0.00–0.12) ceramics sintered in controlled atmosphere.

composition (x)	Cubic $Li_{2+x}Mg_3SnO_6$ (Z = 1/2)			Cubic Mg_2SnO_4 (Z = 8)			R_{wp} (%)	R_p (%)	x^2
	a = b = c (Å)	V (Å^3)	M_1 (%)	a = b = c (Å)	V (Å^3)	M_2 (%)			
0.00	2.1242	76.663	95.81(2)	8.627(1)	642.39(4)	4.18(8)	5.92	3.78	2.453
0.04	2.1231	76.601	98.71(1)	8.621(4)	641.17(4)	1.28(7)	5.85	3.68	2.341
0.08	2.1227	76.517	100	–	–	–	6.06	3.98	2.114
0.12	2.1232	76.566	100	–	–	–	6.22	4.18	2.227

a, b, c, unit cell parameters; V-cell volume; M- weight fraction; R_{wp}-reliability factor of weighted patterns, R_p- reliability factor of patterns, $\times^2$-goodness of fit indicator.

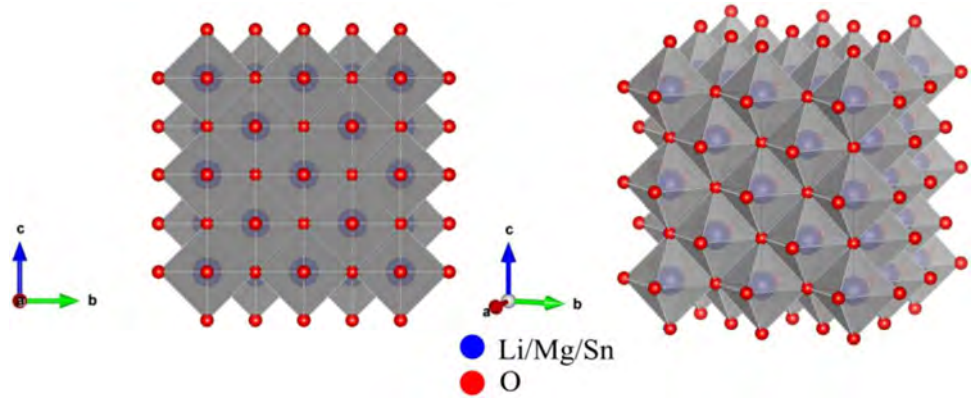

Fig. 6. Schematic illustration of $Li_{2+x}Mg_3SnO_6$ ceramic (x = 0.08) with typical rock-salt structure (2 × 2 × 2).

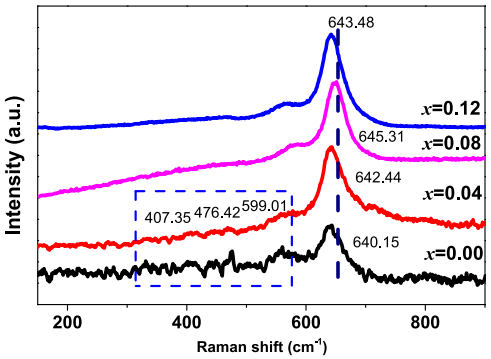

Fig. 7. Raman spectra of $Li_{2+x}Mg_3SnO_6$ (x = 0.00–0.12)) ceramics sintered at optimal temperatures in controlled atmosphere for 5 h.

Table 3
The EDX data of LxMS ceramics marked in Fig. 8.

Spot	Atom (%)			
	Mg	Sn	O	Mg: Sn
A	27.15	13.47	59.38	2.02: 1
B	34.84	11.37	53.79	3.06: 1
C	35.24	12.42	52.34	2.84: 1
D	33.26	11.13	55.61	2.98: 1
E	34.08	12.11	53.81	2.82: 1
F	33.56	11.23	55.21	2.99: 1

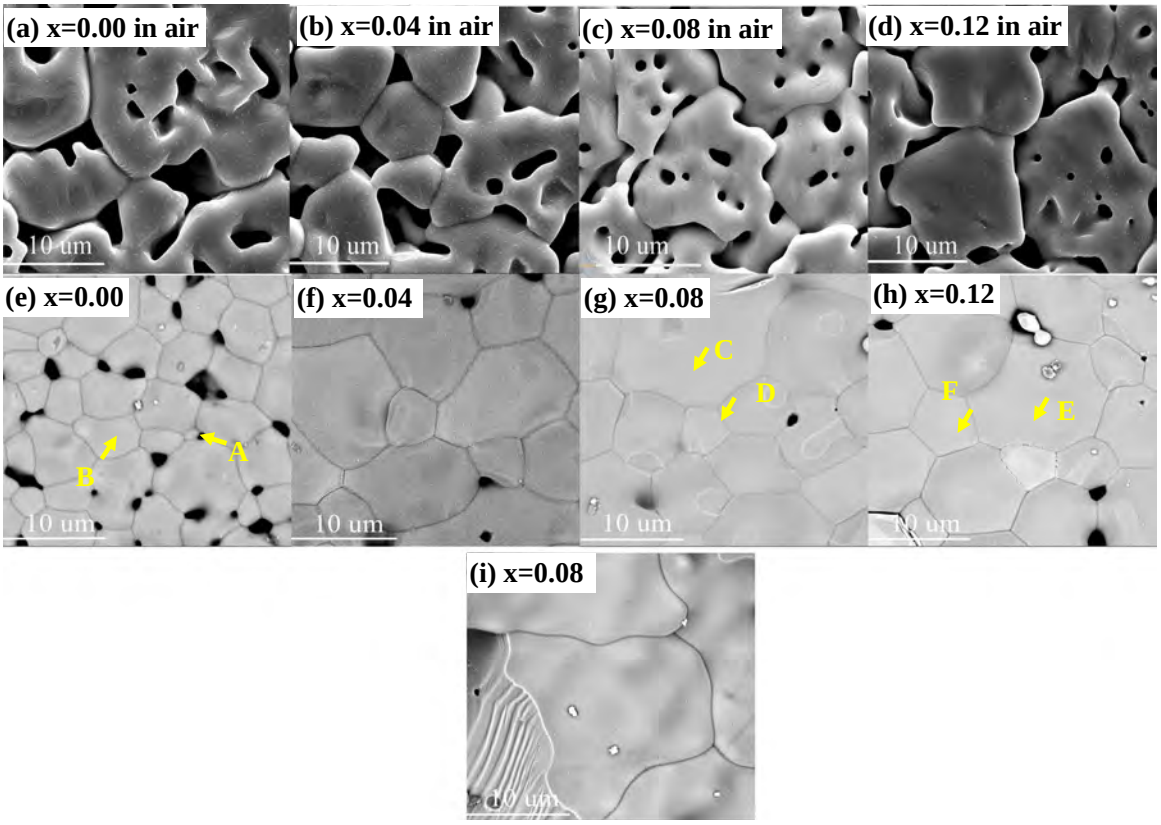

Fig. 8. SEM of surface images of corresponding $Li_{2+x}Mg_3SnO_6$ (x = 0.00–0.12) ceramics sintered at 1350 °C for 5 h in air with (a) x = 0.00, (b) x = 0.04, (c) x = 0.08, (d) x = 0.12; SEM images of thermally etched surface of LxMS ceramics sintered at optimal temperatures for 5 h in controlled atmosphere with (e) x = 0.00, (f) x = 0.04, (g) x = 0.08, (h) x = 0.12; SEM images of fractured surface for x = 0.08 in controlled atmosphere (i).

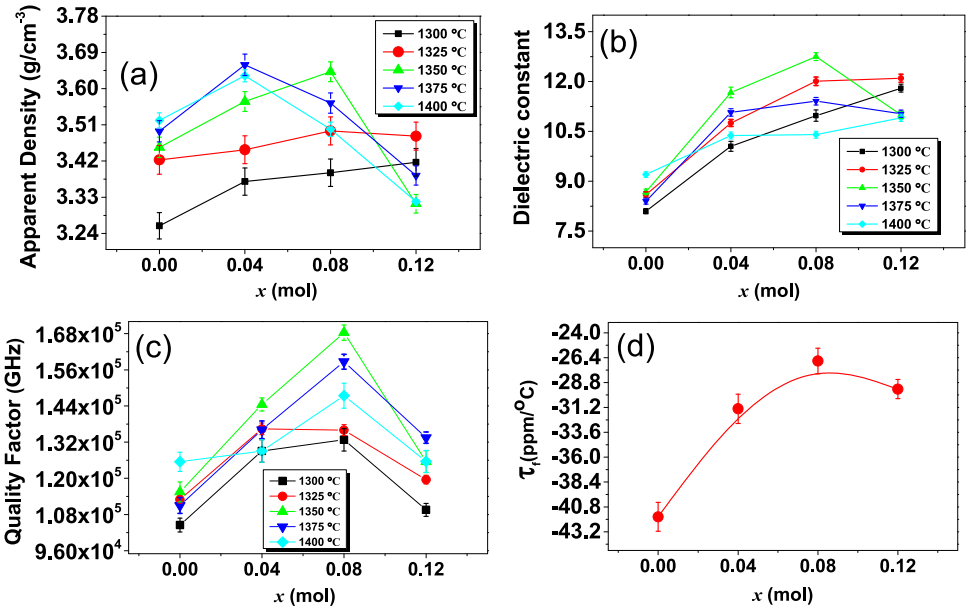

Fig. 9. (a) Apparent density, (b) Dielectric constant (c) Quality factor and (d) Temperature coefficient of resonant frequency of $Li_{2+x}Mg_3SnO_6$ (x = 0.00–0.12) sintered at 1300–1400 °C for 5 h.

Table 4
The bulk density, theoretical density, and relative density of LxMS ceramics sintered at their optimal temperatures as a function of excess lithium content (x).

x	Optimal sintering temperature (°C)	Apparent density (g/cm^3)	Theoretical density (g/cm^3)	Relative density (%)
0.00	1400	3.51	3.81	92.2
0.04	1375	3.58	3.79	94.7
0.08	1350	3.66	3.75	97.6
0.12	1325	3.48	3.64	95.6

For $0.00 \le x \le 0.04$, the theoretical density of the LxMS ceramics was calculated using the equation, $\rho_{theo} = \frac{\rho_1 v_1 + \rho_2 v_2}{v_1 + v_2}$, where v_1 and v_1 were the volume percentage of $Li_2Mg_3SnO_6$ and Mg_2SnO_4 with densities ρ_1 and ρ_2, respectively. And for $0.08 \le x \le 0.12$, the theoretical density of the LxMS ceramics was calculated using the equation, $\rho_{theo} = \frac{nA}{VN_A}$, where n was the number of atoms associated with unit cell, A was the atomic weight, V was the volume of unit cell and N_A was the Avogadro's number.

matrix grains were considered to be $Li_2Mg_3SnO_6$ phase, and small oval grain should be the Mg_2SnO_4 phase, which was consistent with the XRD results.

Fig. 9a displays the apparent density of $Li_{2+x}Mg_3SnO_6$ (x = 0.00–0.12) sintered at 1300–1400 °C in controlled atmosphere for 5 h. The relative density was calculated to better understand the densification process. Table 4 summarizes the relative density of LxMS ceramics sintered at their optimal temperatures as a function of additional lithium (x). According to Fig. 9a, the apparent density for x = 0.00 increased from 3.25 g/cm^3 to 3.51 g/cm^3 because the density of Mg_2SnO_4 (4.62 g/cm^3 at 1550 °C) [11] was larger than that of $Li_2Mg_3SnO_6$ (3.75 g/cm^3 at 1350 °C) [10] with temperature from 1300 °C to 1400 °C. As shown in Table 4, the improvement of relative density 92.2–97.6% was due to the elimination of secondary phase and pores in the region of 0.00–0.08, but when excessive Li were added (0.08–0.12), the relative density decreased to 95.6% because of the increase of cell volume [30]. It was clear that additional lithium contents were beneficial for the sintering process, and reduced the optimal sintering temperature of samples from 1400 °C to 1325 °C. This finding might be resulted from the additional lithium contents and disappearance of Mg_2SnO_4 phase (1550 °C).

The changes of the dielectric constant of LxMS ceramics versus the sintering temperature and lithium content are shown in Fig. 9b. The dielectric constant sintered at their optimal temperatures was effectively improved from 9.2 to 12.7 for $0.00 \le x \le 0.08$, but it slightly decreased to 11.9 for $0.08 < x \le 0.12$. Generally, the dielectric constant relies on the relative density, dielectric polarizabilities and impurity phase [14,31,32]. For $0.00 \le x \le 0.08$, the pores and Mg_2SnO_4 phase were effectively suppressed by the additional lithium content. Thus, the improvement of dielectric constant was mainly attributable to the increasing relative density and the elimination of Mg_2SnO_4 (ε_r = 8.41). For $0.08 \le x \le 0.12$, the influences of porosity could be negligible due to the single $Li_2Mg_3SnO_6$ phase and high relative density (≥95%). Thus in the range of 0.08~0.12,the dielectric constant should be related to the variation of dielectric polarizabilities, and we calculated the dielectric polarizabilities of the samples according to the Clausius–Mossotti formula [31],

$$\alpha_D = \frac{3V_m(\varepsilon_r - 1)}{4\pi(\varepsilon_r + 2)}. \quad (9)$$

In Eq. (9), the ε_r, V_m and α_D represented the dielectric constant, molar volume, and polarizability, respectively. The polarizability (α_D) of samples showed a decrease from 29.07 at x = 0.08 to 28.68 at x = 0.12, leading to the decrease of dielectric constant.

Fig. 9c demonstrates the $Q \times f$ values of LxMS ceramics as a function of the sintering temperature and lithium content. At a given concentration of lithium, the change of $Q \times f$ values were similar to that of apparent densities as a function of sintering temperature. And these variations were considered to relate with the densifications; a higher $Q \times f$ value was usually related to a high densification [33]. The $Q \times f$ values also highly depended on the lithium contents. As shown in Fig. 9c, there was a sharp increase of $Q \times f$ value from 128,778 GHz at x = 0.00 to 168,330 GHz at x = 0.08, but it dropped to 143,449 GHz at x = 0.12. For the microwave dielectric materials, the dielectric loss is usually influenced by the relative density, secondary phase, bond valence, octahedral distortion, packing fraction and the FWHM of vibration mode [9,22,23,25,34]. Thus, for $0.00 \le x \le 0.08$,the improvement of relative density and suppression of Mg_2SnO_4 (55,100 GHz) primarily contributed to the significant enhancement of $Q \times f$ value. Secondly, the FWHM of Raman spectra was proportional to damping coefficient of the structural vibration, indicating that the large FWHM value was related to the high intrinsic loss [22]. Thus, the decrease of high intrinsic loss also improved the quality factor since the FWHM value decreased ranging from 38.72 cm^{-1} to 35.87 cm^{-1}. For

Table 5
The bond valence (V_{bv}), octahedral distortion (δ) and packing fraction for $0.08 \le x \le 0.12$.

Composition	Bond type	d_{ij} (Å)	R_{ij} (Å)	δ (10^{-4})	$V_{Li,\ Mg,Sn-O}$	Packing fraction (%)
x = 0.08	Li-O	2.1227	1.466	0.0015	1.017	51.43
	Mg-O	2.1227	1.693	0.0015	1.878	
	Sn-O	2.1227	1.905	0.0015	3.332	
x = 0.12	Li-O	2.1232	1.466	0.0019	1.015	51.39
	Mg-O	2.1232	1.693	0.0019	1.875	
	Sn-O	2.1232	1.905	0.0019	3.326	

$0.08 \le x \le 0.12$, the intrinsic factors should mainly be responsible for the deterioration of quality factor because of the single phase and high relative density (>95%). The $Q \times f$ value was primarily influenced by the following intrinsic losses: bond valence (V_{bv}), octahedral distortion (δ), packing fraction and FWHM. In the range of 0.08–0.12, bond valence (V_{bv}) octahedral distortion (δ) and packing fraction were calculated from the classical Eqs. (10)–(13) [4,31,34,35].

$$V_i = \sum_{i=1}^{n=j} v_{ij} \tag{10}$$

$$v_{ij} = \exp\left(\frac{R_{ij} - d_{ij}}{b'}\right) \tag{11}$$

$$\delta = \frac{(\text{B} - \text{O distance}_{largest}) - (\text{B} - \text{O distance}_{smallest})}{\text{B} - \text{O distance}_{average}} \tag{12}$$

$$\text{Packing fraction}(\%) = \frac{volume\ of\ the\ atoms\ in\ the\ cell}{volume\ of\ the\ unit\ cell} \times Z \tag{13}$$

In Eqs. (10)–(12), the bond valence parameters, R_{ij}, are obtained from Brese's study, while d_{ij} is the length of the bond between atom i and j from the refined result, and b' is commonly considered as 0.37 Å. In Eq. (13), Z is the number of formula units per unit cell. Table 5 summarizes bond valence ($V_{Li,\ Mg,Sn-O}$), octahedral distortion (δ) and packing fraction for $0.08 \le x \le 0.12$. It was remarkable that three kinds of bond valence (V_{Li-O}, V_{Mg-O} and V_{Sn-O}) had different degrees of decrease, and the V_{Sn-O} sharply decreased from 3.332 to 3.326. Meanwhile, the packing fraction was reduced from 51.43% to 51.39%, the lattice vibrations increased, and the quality factors decreased correspondingly. Moreover, the FWHM of Raman spectrum also increased from 35.87 cm^{-1} to 36.16 cm^{-1}, leading to the increase of the damping characteristics. The quality factor was inversely proportional to the FWHM in whole composition range, which were consistent with other reports about the researches of damping character for microwave propagation in dielectric ceramics [22,23,25,36].

Fig. 9d displays the τ_f of the LxMS ceramics as a function of lithium contents sintered at optimal temperatures for 5 h. The τ_f initially increased from −41.7 at x = 0.00 to −27.4 ppm/°C at x = 0.08, later decreased to −30.1 ppm/°C at x = 0.12. It is well known that the τ_f shows a high dependence on the phase composition, bond valence (V_{bv}) and octahedral distortion (δ) [4,34,35]. For $0.00 \le x \le 0.08$, the elimination of Mg_2SnO_4 (−62 ppm/°C) effectively contributed to the improvement of τ_f. However, the deterioration of τ_f values should be caused by the decrease of three kinds of bond valence (V_{Li-O}, V_{Mg-O} and V_{Sn-O}), as shown in Table 5. What's more, the octahedral distortion (δ) was believed to be associated with τ_f value. It was clear that when the excess lithium contents were increased from 0.08 to 0.12, the δ changed from 0.0015×10^{-4} to 0.0019×10^{-4}, and the τ_f correspondingly varied from −27.4 ppm/°C to −30.1 ppm/°C. As a result, both of the bond valence and octahedral distortion should be taken into consideration during this range.

In summary, the atmosphere-controlled sintering was employed to prepare the $Li_{2+x}Mg_3SnO_6$ ceramics. When the extra lithium concentration was 0.08, the LxMS ceramics sintered in controlled atmosphere at 1350 °C for 5 h possessed excellent comprehensive properties of ε_r = 12.7, $Q \times f$ = 168,330 GHz and τ_f = −27.4 ppm/°C. Both of the surface image and the fractured photograph of LxMS for x = 0.08 showed a highly dense microstructure with good grains and clear boundaries, and the secondary phases could be completely eliminated because of the critical roles of protective atmosphere and additional lithium contents. Besides of the high relative densities, our current achievement was much better than our former works of microwave dielectric properties of $Li_{2+x}Mg_3SnO_6$ (x = 0.00, 0.04, 0.08, 0.12 and 0.25) ceramics sintered in air, as shown in Table 1. Hence, this novel sintering method was meaningful for the preparation of lithium containing ceramics in high temperature.

4. Conclusions

The novel atmosphere controlled sintering was employed to prepare the $Li_{2+x}Mg_3SnO_6$ (x = 0.00–0.12) ceramics using solid-state reaction technique, and the influences of additional lithium contents on the phase evolution, crystal structures and microwave dielectric characteristics of $Li_{2+x}Mg_3SnO_6$ ceramics were systematically studied. As the calcination temperature was 700 °C, the Li_2SnO_3 phase with monoclinic rock salt structure in C2/c space group was obtained for the first time. The $Li_2Mg_3SnO_6$ phase formed from the chemical reactions between Li_2SnO_3 and MgO in the temperature range of 800–1000 °C. Pure $Li_2Mg_3SnO_6$ phase with cubic rock salt structure in $Fm\bar{3}m$ could be observed in the samples calcinated at 1000–1100 °C. As the calcination temperature was over 1100 °C, the $Li_2Mg_3SnO_6$ phase decomposed into Mg_2SnO_4, MgO and Li_2O. When the green samples sintered in the controlled atmosphere, the phase compositions, crystal structures and microwave dielectric properties were highly dependent on the additional lithium in LxMS systems. The relationship between the phase compositions, crystal structures and microwave dielectric properties were investigated on the basis of the Rietveld refinement, bond valence and Raman spectra theory. Because of the controlled-atmosphere and extra lithium contents, the ε_r, $Q \times f$ and τ_f were significantly improved by the suppression of secondary phase and pores for $0.00 \le x \le 0.08$. However, the comprehensive microwave property was deteriorated when excess lithium contents were added ($0.08 < x \le 0.12$), which were correlated with dielectric polarization, bond valence, FWHM, packing fraction and octahedral distortion. Typically, the excellent microwave properties of $Li_{2+x}Mg_3SnO_6$ (x = 0.08) sintered at 1350 °C in novel atmosphere controlled atmosphere were achieved: ε_r = 12.7, $Q \times f$ = 168,330 GHz and τ_f = −27.4 ppm/°C.

Acknowledgements

This work was supported by the National Natural Science Foundation of China (Grant No. 51402039 and 51672038) and by Open Foundation of National Engineering Research Center of Electromagnetic Radiation Control Materials (ZYGX2016K003-5). Zixuan Fang gratefully acknowledged support from the China Scholarship Council (CSC, 201706070025) during a visiting study at the University of California, Berkeley.

Appendix A. Supplementary material

Supplementary data associated with this article can be found in the online version at http://dx.doi.org/10.1016/j.ceramint.2017.07.074.

References

[1] I.M. Reaney, D. Iddles, Microwave dielectric ceramics for resonators and filters in mobile phone networks, J. Am. Ceram. Soc. 89 (7) (2006) 2063–2072.
[2] M.T. Sebastian, Dielectric Materials For Wireless Communication, first ed., Elsevier Science, Amsterdam, 2008.
[3] M.T. Sebastian, R. Ubic, H. Jantunen, Microwave Materials and Applications, John Wiley & Sons, 2017.

[4] Z.-X. Fang, B. Tang, E. Li, S.-R. Zhang, High-Q microwave dielectric properties in the $Na_{0.5}Sm_{0.5}TiO_3$ + Cr_2O_3 ceramics by one synthetic process, J. Alloy. Compd. 705 (2017) 456–461.
[5] A. Osseiran, F. Boccardi, V. Braun, K. Kusume, P. Marsch, M. Maternia, O. Queseth, M. Schellmann, H. Schotten, H. Taoka, H. Tullberg, M.A. Uusitalo, B. Timus, M. Fallgren, Scenarios for 5G mobile and wireless communications: the vision of the METIS project, IEEE Commun. Mag. 52 (5) (2014) 26–35.
[6] D. Zhou, L.-X. Pang, J. Guo, Z.-M. Qi, T. Shao, Q.-P. Wang, H.-D. Xie, X. Yao, C.A. Randall, Influence of Ce Substitution for Bi in BiVO4 and the Impact on the Phase Evolution and Microwave Dielectric Properties, Inorg. Chem. 53 (2) (2014) 1048–1055.
[7] L.-X. Pang, D. Zhou, Z.-M. Qi, W.-G. Liu, Z.-X. Yue, I.M. Reaney, Structure-property relationships of low sintering temperature scheelite-structured (1 - x) $BiVO_4$-x$LaNbO_4$ microwave dielectric ceramics, J. Mater. Chem. C 5 (10) (2017) 2695–2701.
[8] Z. Fang, B. Tang, F. Si, S. Zhang, Temperature stable and high-Q microwave dielectric ceramics in the $Li_2Mg_{3-x}Ca_xTiO_6$ system (x = 0.00–0.18), Ceram. Int. 43 (2) (2017) 1682–1687.
[9] H. Wu, E.S. Kim, Correlations between crystal structure and dielectric properties of high-Q materials in rock-salt structure Li_2O–MgO–BO_2 (B = Ti, Sn, Zr) systems at microwave frequency, RSC Adv. 6 (53) (2016) 47443–47453.
[10] Z. Fu, P. Liu, J. Ma, X. Zhao, H. Zhang, Novel series of ultra-low loss microwave dielectric ceramics: $Li_2Mg_3BO_6$ (B = Ti, Sn, Zr), J. Eur. Ceram. Soc. 36 (3) (2016) 625–629.
[11] Y.-C. Chen, Y.-N. Wang, C.-H. Hsu, Elucidating the dielectric properties of Mg_2SnO_4 ceramics at microwave frequency, J. Alloy. Compd. 509 (40) (2011) 9650–9653.
[12] J.J. Bian, Y.F. Dong, New high Q microwave dielectric ceramics with rock salt structures: (1 − x)Li_2TiO_3+xMgO system (0 ≤ x ≤ 0.5), J. Eur. Ceram. Soc. 30 (2) (2010) 325–330.
[13] Z. Fu, P. Liu, J. Ma, B. Guo, X. Chen, H. Zhang, Microwave dielectric properties of low-fired Li_2SnO_3 ceramics co-doped with MgO–LiF, Mater. Res. Bull. 77 (2016) 78–83.
[14] G.-h. Chen, C.-l. Yuan, C.-r. Zhou, Y. Yang, Low-firing high permittivity $Ca_{0.6}Sm_{0.8/3}TiO_3$–$(Li_{0.5}Nd_{0.5})TiO_3$ ceramics with $BaCu(B_2O_5)$ addition, Ceram. Int. 39 (8) (2013) 9763–9766.
[15] L.-X. Pang, D. Zhou, Microwave dielectric properties of low-firing Li_2MO_3 (M = Ti, Zr, Sn) ceramics with B_2O_3–CuO addition, J. Am. Ceram. Soc. 93 (11) (2010) 3614–3617.
[16] B. Toby, EXPGUI, a graphical user interface for GSAS, J. Appl. Crystallogr. 34 (2) (2001) 210–213.
[17] J.P. Kruth, G. Levy, F. Klocke, T.H.C. Childs, Consolidation phenomena in laser and powder-bed based layered manufacturing, CIRP. Ann.-Manuf. Technol. 56 (2) (2007) 730–759.
[18] O.-.H. Kwon, C. Coureau, R.A. Gorski, M.A. Simpson, Zirconia Toughened Alumina ESD Safe Ceramic Composition, Component, and Methods for Making Same, US Patents, 2007.
[19] M. Castellanos, A.R. West, Order-disorder phenomena in oxides with rock salt structures: the system Li_2TiO_3-MgO, J. Mater. Sci. 14 (2) (1979) 450–454.
[20] Rt Shannon, Revised effective ionic radii and systematic studies of interatomic distances in halides and chalcogenides, Acta Crystallogr. Sect. A 32 (5) (1976) 751–767.
[21] J.J. Bian, Y.F. Dong, Sintering behavior, microstructure and microwave dielectric properties of $Li_{2+x}TiO_3$ (0 ≤ x ≤ 0.2), Mater. Sci. Eng. B 176 (2) (2011) 147–151.
[22] M.Y. Chen, C.T. Chia, I.N. Lin, L.J. Lin, C.W. Ahn, S. Nahm, Microwave properties of $Ba(Mg_{1/3}Ta_{2/3})O_3$, $Ba(Mg_{1/3}Nb_{2/3})O3$ and $Ba(Co_{1/3}Nb_{2/3})O_3$ ceramics revealed by Raman scattering, J. Eur. Ceram. Soc. 26 (10–11) (2006) 1965–1968.
[23] S.J. Webb, J. Breeze, R.I. Scott, D.S. Cannell, D.M. Iddles, N.M. Alford, Raman spectroscopic study of gallium-doped $Ba(Zn_{1/3}Ta_{2/3})O_3$, J. Am. Ceram. Soc. 85 (7) (2002) 1753–1756.
[24] M. Popa, J. Frantti, M. Kakihana, Characterization of LaMeO3 (Me: mn, Co, Fe) perovskite powders obtained by polymerizable complex method, Solid. State Ion. 154–155 (2002) 135–141.
[25] A. Dias, L.A. Khalam, M.T. Sebastian, C.W.A. Paschoal, R.L. Moreira, Chemical substitution in $Ba(RE_{1/2}Nb_{1/2})O_3$ (RE = La, Nd, Sm, Gd, Tb, and Y) microwave ceramics and its influence on the crystal structure and phonon modes, Chem. Mater. 18 (1) (2006) 214–220.
[26] S. George, M.T. Sebastian, Synthesis and microwave dielectric properties of novel temperature stable high Q, $Li_2ATi_3O_8$ (A = Mg, Zn) ceramics, J. Am. Ceram. Soc. 93 (8) (2010) 2164–2166.
[27] S. George, M.T. Sebastian, Microwave dielectric properties of novel temperature stable high Q $Li_2Mg_{1-x}ZnxTi_3O_8$ and $Li_2A_{1-x}Ca_xTi_3O_8$ (A = Mg, Zn) ceramics, J. Eur. Ceram. Soc. 30 (12) (2010) 2585–2592.
[28] Y. Iida, Evaporation of lithium oxide from solid solution of lithium oxide in nickel oxide, J. Am. Ceram. Soc. 43 (3) (1960) 171–172.
[29] N.-X. Xu, J.-H. Zhou, H. Yang, Q.-L. Zhang, M.-J. Wang, L. Hu, Structural evolution and microwave dielectric properties of MgO–LiF co-doped Li_2TiO_3 ceramics for LTCC applications, Ceram. Int. 40 (2014) 15191–15198.
[30] R.C. Pullar, J.D. Breeze, N.M. Alford, Characterization and microwave dielectric properties of $M^{2+}Nb_2O_6$ ceramics, J. Am. Ceram. Soc. 88 (9) (2005) 2466–2471.
[31] Y. Zhao, P. Zhang, High-Q microwave dielectric ceramics using $Zn_3Nb_{1.88}Ta_{0.12}O_8$ solid solutions, J. Alloy. Compd. 662 (2016) 455–460.
[32] E.S. Kim, D.H. Kang, J.M. Yang, H.S. Shin, N.I. Zahari, H. Ohsato, Crystal structure and dielectric properties of $Ca_{0.85}Nd_{0.1}TiO_3$-$LnAlO_3$(Ln = Sm, Gd, Dy, Er) ceramics, in: Proceedings of the Sixteenth IEEE International Symposium on Applications of Ferroelectrics, ISAF 2007, 2007, pp. 523–524.
[33] S.H. Yoon, G.-K. Choi, D.-W. Kim, S.-Y. Cho, K.S. Hong, Mixture behavior and microwave dielectric properties of (1 − x)$CaWO_4$–xTiO_4, J. Eur. Ceram. Soc. 27 (8–9) (2007) 3087–3091.
[34] J. Li, Y. Han, T. Qiu, C. Jin, Effect of bond valence on microwave dielectric properties of (1 − x)$CaTiO_3$–x$(Li_{0.5}La_{0.5})TiO_3$ ceramics, Mater. Res. Bull. 47 (9) (2012) 2375–2379.
[35] T. Hirata, Oxygen Position, Octahedral Distortion, and Bond-Valence Parameter from Bond Lengths in $Ti_{1-x}Sn_xO_2$ (0 ≤x≤ 1), J. Am. Ceram. Soc. 83 (12) (2000) 3205–3207.
[36] S.K. Singh, V.R.K. Murthy, Crystal structure, Raman spectroscopy and microwave dielectric properties of layered-perovskite $BaA_2Ti_3O_{10}$ (A = La, Nd and Sm) compounds, Mater. Chem. Phys. 160 (2015) 187–193.